SUPPLEMENTARY INFORMATION

Efficient prediction of highly anisotropic excitonic properties in the layered antiferromagnet CrSBr via time-dependent density functional theory

Ashwin Ramasubramaniam,[1,2,*] **Daniel Hernangómez-Pérez,**[3] **Javier Junquera,**[4] **María Camarasa-Gómez**[5]

[1] Department of Mechanical and Industrial Engineering, University of Massachusetts, Amherst, MA 01003, U.S.A.

[2] Graduate Program in Materials Science and Engineering, University of Massachusetts, Amherst, MA 01003, U.S.A.

[3] CIC nanoGUNE BRTA, Tolosa Hiribidea 76, 20018 San Sebastián, Spain

[4] Departamento de Ciencias de la Tierra y Física de la Materia Condensada, Facultad de Ciencias, Universidad de Cantabria, Avenida de los Castros s/n, E-39005 Santander, Spain

[5] Centro de Física de Materiales (CFM-MPC), CSIC-UPV/EHU, Paseo Manuel de Lardizabal 5 20018 Donostia-San Sebastián, Spain

Corresponding Author

* ashwin@engin.umass.edu

S1. SUPPORTING FIGURES FOR GLOBAL AND RANGE-SEPARATED HYBRIDS

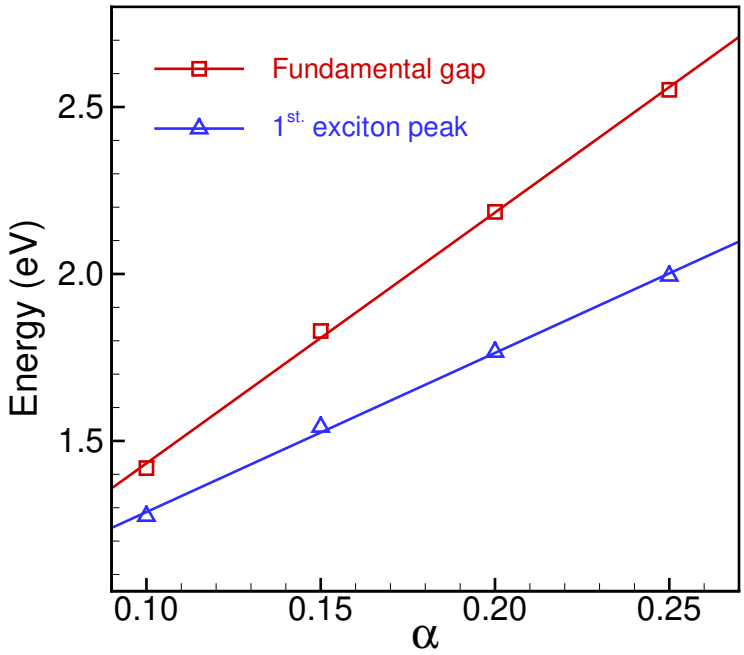

Figure S1: Fundamental gap and energy of first exciton peak as a function of global fraction of exact exchange, α.

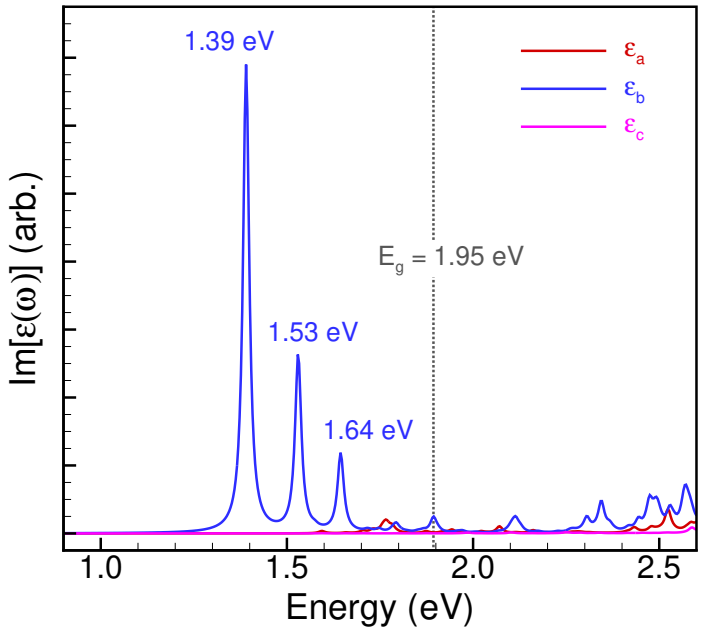

Figure S2: Optical spectrum (imaginary part of frequency-dependent dielectric function) for a range-separated hybrid with short-range fraction of exact exchange α=0.1, long-range fraction of exact-exchange β=0.3, and range-separation parameter γ=0.2 $Å^{-1}$.

S2. UNIT CELL AND ATOMIC COORDINATES (VASP POSCAR)

Atomic positions and lattice parameters from Ref. 1.

```
Cr S Br AFM bulk
1.0
        3.5120599270         0.0000000000         0.0000000000
        0.0000000000         4.7447900772         0.0000000000
        0.0000000000         0.0000000000        15.8240995407
   Cr    S   Br
    4    4    4
Direct
0.750000000  0.250000000  0.564059973
0.750000000  0.250000000  0.064059973
0.250000000  0.750000000  0.435940027
0.250000000  0.750000000  0.935940027
0.750000000  0.750000000  0.538500011
0.750000000  0.750000000  0.038500011
0.250000000  0.250000000  0.461499989
0.250000000  0.250000000  0.961499989
0.750000000  0.750000000  0.323599994
0.750000000  0.750000000  0.823599994
0.250000000  0.250000000  0.676400006
0.250000000  0.250000000  0.176400006
```

S3. PARAMETRIC DEPENDENCE OF FUNDAMENTAL GAPS AND EXCITON ENERGIES ON α AND V_W

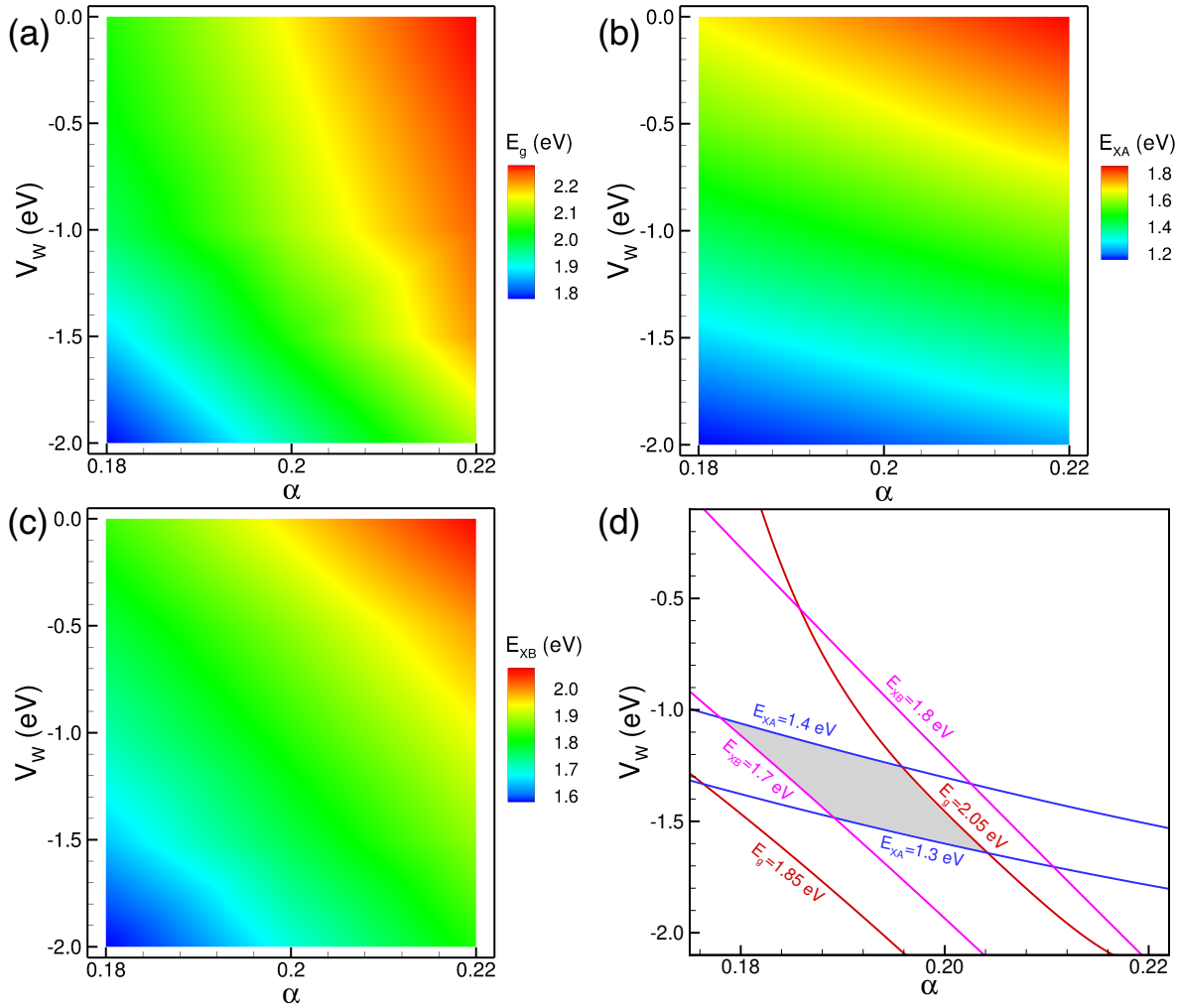

Figure S3: Contour plots depicting the dependence of (a) the fundamental gap, E_g, (b) the X_A exciton energy, and (c) the X_B exciton energy on the fraction of global exact exchange α and the onsite correction, V_w, applied to Cr *d*-orbitals. (d) Contours of E_g (red lines), X_A (blue lines), and X_B (magenta lines) superposed to find the space of feasible solutions (grey region) for α and V_w. The limiting values of E_g are 1.85 eV and 2.05 eV (as explained in the main text); for the X_A and X_B exciton energies, we use narrow 10-meV windows of uncertainty ranging from 1.3-1.4 eV and 1.7-1.8 eV, respectively.

The two independent parameters α and V_w can be determined efficiently by performing a parameter sweep in α–V_w space and recording the fundamental gap (E_g) as well as the X_A and X_B exciton energies. Figures S3(a-c) display these data for E_g, and X_A and X_B exciton energies, which can then be combined with known bounds from the literature to identify a space of feasible solutions [Fig. S3(d)]. Interestingly, if we reply purely on the energies of the X_A and X_B excitons – to which we apply a small 10-meV window of uncertainty – the fundamental gap is consistently

predicted to be above the ARPES lower bound of 1.85 eV. At the upper end, the fundamental gap is bounded by 2.10 eV, which is only slightly above the theoretical $QSG\widehat{W}$ value of ~2.05 eV. If we enforce precise values of 1.36 eV and 1.76 eV for the X_A and X_B excitons, respectively, the fundamental gap is predicted to be 2.02 eV, within expected bounds.

The parameter sweeps displayed here were carried out without spin-orbit coupling; time-dependent calculations of the optical spectrum were carried out using 16 occupied and 16 empty states, which is sufficient to converge the energy of the X_B exciton to within 5 meV and that of the X_A exciton to ~40 meV. Having identified a reasonable window of parameter space, more targeted and computationally expensive calculations with spin-orbit coupling can be performed to identify a suitable α and V_w, selected results for which are displayed in Figure 2 of the main article.

It is noteworthy that the tuning process can rely almost entirely on high-quality optical measurements at low temperatures that are much less involved than low-temperature ARPES measurements.

S4. EXCITON FATBAND PLOTS

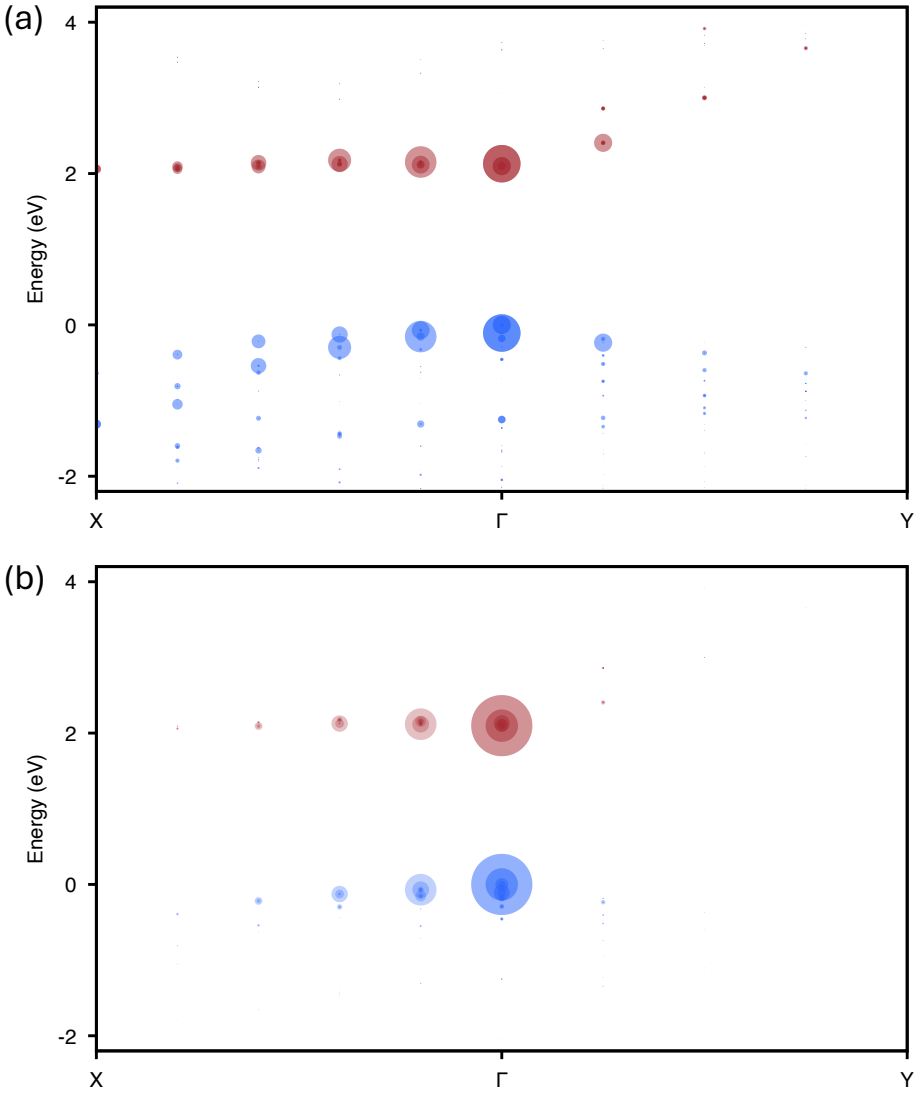

Figure S4: Fatband plots for the (a) X_A and (b) X_B excitons of the bulk AFM phase. Blue and red circles indicate valence and conduction states with their radii representing the coupling strength. The valence band edge energy is set to zero. Fatband plots are converted to heatmaps (Figure 3 of manuscript) by a standard rasterization process, using a 500×700 *k*-point–energy grid and a Gaussian smoothing of 0.02 in both dimensions to produce a 2D intensity map that is finally normalized (between 0 and 1) and overlaid on the bandstructure.

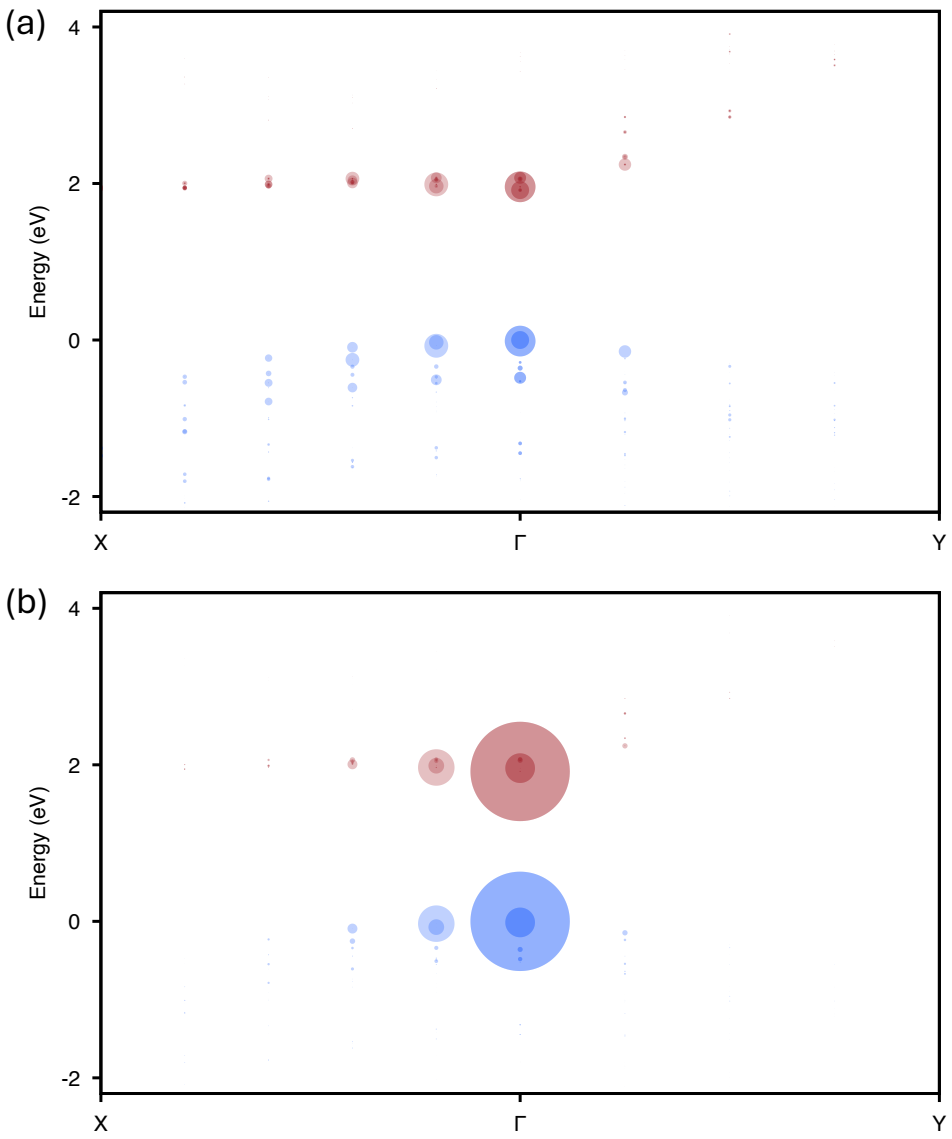

Figure S5: Same as Figure S4 except for the c-FM bulk phase.

S5. HYBRID+V_W TESTS WITH SIESTA

To confirm that conclusions drawn from the hybrid+V_w calculations in VASP are not a result of artifacts, we performed a complementary set of selected tests with another first-principles code SIESTA. The SIESTA calculations were performed using the PBE0 hybrid functional, employing the standard 25% fraction of Hartree–Fock exchange.[2] The implementation of this functional within the numerical atomic-orbital framework of SIESTA has been carried out only recently.[3,4]

Core electrons were replaced by *ab initio* norm-conserving fully separable pseudopotentials.[5] In this work the optimized norm-conserving Vanderbilt pseudopotentials proposed by Hamann [6] were used, in the PSML[7] format available in the Pseudo-Dojo periodic table.[8,9] For Cr, the semicore 3*s* and 3*p* electrons were explicitly included in the valence. For Br, the semicore 3*d* shell was also considered. For S, the valence configuration was made of the 3*s* and 3*p* orbitals. In the generation of the pseudopotentials, the exchange-correlation functional was approximated using the Perdew-Burke-Ernzerhof (PBE) functional.[10]

The one-electron Kohn-Sham eigenstates were expanded in a basis of strictly localized [11] numerical atomic orbitals.[12] The native basis functions were obtained by finding the eigenfunctions of the isolated atoms confined within the soft-confinement spherical potential proposed in Ref. 13. A single-ζ basis set was applied to the 3*s* and 3*p* semicore states of Cr, and for the 3*d* semicore states of Br. For the valence states of Cr, S, and Br, we used a basis of double-ζ polarized quality, with all the parameters controlling the range and the shape taken from default. In the hybrid-functional implementation of SIESTA, the native numerical atomic orbitals are replaced by a fitted expansion in Gaussian functions. The maximum number of Gaussians in this expansion was set to four, and the contracted sum was truncated at the radius where r^l times the Gaussian combination falls below 5×10^{-3}. The threshold used to screen four-center integrals via the Schwarz inequality was fixed to 1×10^{-6}. In addition to the hybrid functional, we included an onsite correction on the Cr 3*d* manifold following the Dudarev formalism.[14] The corresponding atomic projectors were generated using the same procedure employed for the construction of the native basis set, enforcing a tight cutoff radius of 2.5 Bohr.

The electronic density, Hartree, and exchange-correlation potentials, as well as the corresponding matrix elements between the basis orbitals, were calculated in a uniform real space grid.[16] An equivalent plane-wave cutoff of 1200 Ry was used to represent the charge density. The integrals in reciprocal space were well converged, using in all the cases a sampling in reciprocal space of the same quality as the (10×8×2) Monkhorst-Pack mesh.[16] Atomic coordinates and lattice vectors used were the same as those for VASP (Sec. S2).

Figure S6 displays the projected density of states for three cases with $V_w = 0$ eV (no onsite correction) and $V_w = \pm1$ eV. Similar to the results in Figure 2 of the main manuscript, we find that for zero or positive V_w the occupied Cr levels are too deep in the valence band, with the band edge being dominated by anion states. With negative values of V_w, the occupied Cr levels shift towards the valence band edge, and the relative contribution of anion states becomes smaller.

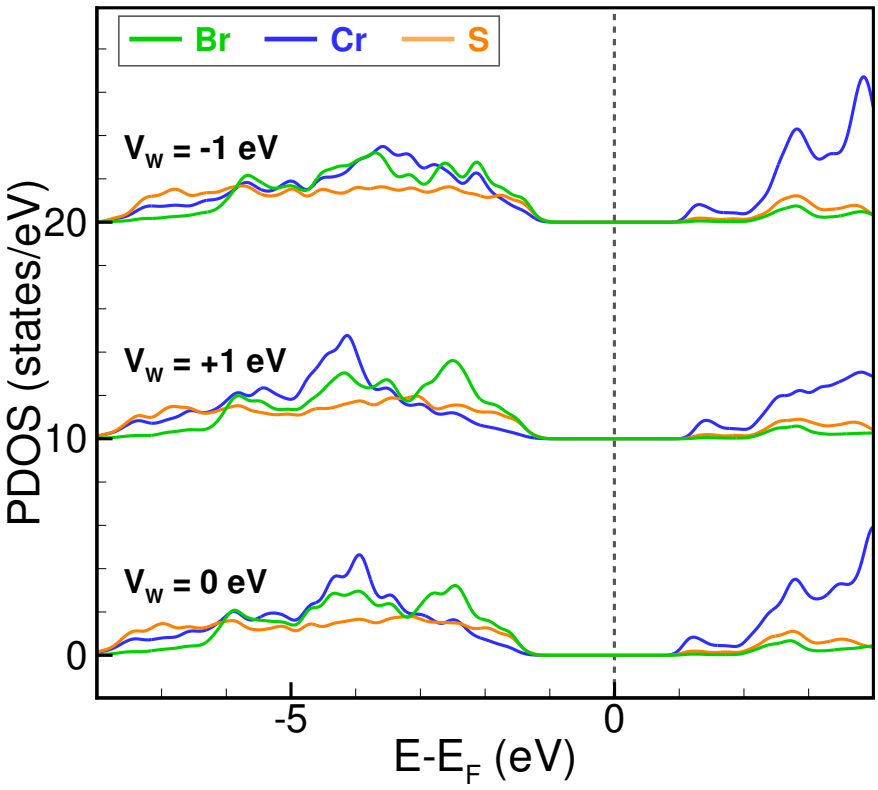

Figure S6: Species-wise PDOS of bulk CrSBr using the hybrid+Vw approach in SIESTA with the PBE0 (a=0.25) global hybrid. The Fermi level is set mid-gap and only the majority spin PDOS are indicated, the minority spin channel being degenerate.

REFERENCES

[1] S. A. López-Paz, Z. Guguchia, V. Y. Pomjakushin, C. Witteveen, A. Cervellino, H. Luetkens, N. Casati, A. F. Morpurgo, and F. O. von Rohr, Dynamic Magnetic Crossover at the Origin of the Hidden-Order in van Der Waals Antiferromagnet CrSBr. Nat. Commun. 13 (1), 4745 (2022).

[2] J. P. Perdew, M. Ernzerhof, and K. Burke, Rationale for mixing exact exchange with density functional approximations, J. Chem. Phys. 105, 9982 (1996).

[3] A. García, N. Papior, A. Akhtar, E. Artacho, V. Blum, E. Bosoni, P. Brandimarte, M. Brandbyge, J. I. Cerdá, F. Corsetti, R. Cuadrado, V. Dikan, J. Ferrer, J. Gale, P. García-Fernández, V. M. García-Suárez, S. García, G. Huhs, S. Illera, R. Korytár, P. Koval, I. Lebedeva, L. Lin, P. López-Tarifa, S. G. Mayo, S. Mohr, P. Ordejón, A. Postnikov, Y. Pouillon, M. Pruneda, R. Robles, D. Sánchez-Portal, J. M. Soler, R. Ullah, V. W.-Z. Yu, and J. Junquera, SIESTA: Recent developments and applications, J. Chem. Phys. 152, 204108 (2020).

[4] Y. Pouillon, B. C. Oyomo, J. Sifuna, M. Camarasa-Gómez, X. Qin, C. Beltrán, F. Gómez-Ortiz, H. Shang, and J. Junquera, Implementation of the hybrid exchange-correlation functionals in the SIESTA code, Comput. Phys. Commun. 323, 110086 (2026).

[5] L. Kleinman and D. M. Bylander, Efficacious form for model pseudopotentials, Phys. Rev. Lett. 48, 1425 (1982).

[6] D. Hamann, Optimized norm-conserving Vanderbilt pseudopotentials, Phys. Rev. B 88, 085117 (2013).

[7] A. García, M. J. Verstraete, Y. Pouillon, and J. Junquera, The PSML format and library for norm-conserving pseudopotential data curation and interoperability, Comput. Phys. Commun. 227, 51 (2018).

[8] M. Van Setten, M. Giantomassi, E. Bousquet, M. J. Verstraete, D. R. Hamann, X. Gonze, and G.-M. Rignanese, The PseudoDojo: Training and grading a 85 element optimized norm-conserving pseudopotential table, Comput. Phys. Commun. 226, 39 (2018).

[9] The scalar relativistic oncvpsp v0.4.1 pseudopotentials with stringent accuracy were used.

[10] J. P. Perdew, K. Burke, and M. Ernzerhof, Generalized gradient approximation made simple, Phys. Rev. Lett. 77, 3865 (1996).

[11] O. F. Sankey and D. J. Niklewski, Ab initio multicenter tight-binding model for molecular-dynamics simulations and other applications in covalent systems, Phys. Rev. B 40, 3979 (1989).

[12] E. Artacho, D. Sánchez-Portal, P. Ordejón, A. García, and J. M. Soler, Linear-scaling ab-initio calculations for large and complex systems, Phys. Stat. Sol. (b) 215, 809 (1999).

[13] J. Junquera, O. Paz, D. Sánchez-Portal, and E. Artacho, Numerical atomic orbitals for linear-scaling calculations, Phys. Rev. B 64, 235111 (2001).

[14] S. L. Dudarev, G. A. Botton, S. Y. Savrasov, C. J. Humphreys, and A. P. Sutton, Electron-energy-loss spec- tra and the structural stability of nickel oxide: An LSDA + U study, Phys. Rev. B 57, 1505 (1998).

[15] J. M. Soler, E. Artacho, J. D. Gale, A. García, J. Junquera, P. Ordejón, and D. Sánchez-Portal, The SIESTA method for ab initio order-N materials simulation, J. Phys.: Condens. Matter 14, 2745 (2002).

[16] H. J. Monkhorst and J. D. Pack, Special points for Brillouin-zone integrations, Phys. Rev. B 13, 5188 (1976).